

# **Significance of the First Excited State Position in Quantum Well Infrared Photodetectors (QWIPs)**

*S. D. Gunapala and S. V. Bandara*

Center for Space Microelectronics Technology, Jet Propulsion Laboratory, California

Institute of Technology, Pasadena, CA 91109, USA

(818) 354-1880 – voice; (818) 393-4540 - fax

## ***ABSTRACT***

An exceptionally rapid progress has been made during last few years in the performance of GaAs/AlGaAs based quantum well infrared photodetectors (QWIPs), starting from bound-to-bound which has relatively lower sensitivity, and culminating in high performance bound-to-quasibound QWIPs. In this paper, we discuss and compare the dependence of absorption, responsivity, dark current, and detectivity of QWIPs with the position of first excited state in the quantum well.

## ***1. INTRODUCTION***

The idea of using MQW structures to detect infrared radiation can be explained by using the basic principles of quantum mechanics. The quantum well is equivalent to the well known particle in a box problem in quantum mechanics, which can be solved by the time independent Schrödinger equation. The solutions to this problem are the Eigen values that describe energy levels inside the quantum well in which the particle is allowed to exist. The position of the energy levels are primarily determined by the quantum well

dimensions (height and width). For infinitely high barriers and parabolic bands, the energy levels in the quantum well are given by [1]

$$E_j = \left( \frac{\hbar^2 \pi^2}{2m^* L_w^2} \right) j^2, \quad (1)$$

where  $L_w$  is the width of the quantum well,  $m^*$  is the effective mass of the carrier in the quantum well, and  $j$  is an integer. Thus the intersubband energy between the ground and the first excited state is

$$(E_2 - E_1) = (3\hbar^2 \pi^2 / 2m^* L_w^2). \quad (2)$$

The quantum well infrared photodetectors (QWIPs) discussed in this article utilize the photoexcitation of electron (hole) between the ground state and the first excited state in the conduction (valance) band quantum well (See Fig. 1). The quantum well structure is designed so that these photoexcited carriers can escape from the quantum well and be collected as photocurrent. In addition to larger intersubband oscillator strength, these detectors afford greater flexibility than extrinsically doped semiconductor infrared detectors because the wavelength of the peak response and cutoff can be continuously tailored by varying layer thickness (quantum well width) and barrier composition (barrier height) [2,3].

The lattice matched GaAs/ $Al_xGa_{1-x}As$  material system is a very good candidate to create such a quantum well structure, because the band gap of  $Al_xGa_{1-x}As$  can be changed continuously by varying  $x$  (and hence the height of the quantum well). Thus, by changing the quantum well width  $L_w$  and the barrier height ( $Al$  molar ratio of  $Al_xGa_{1-x}As$  alloy), this intersubband transition energy can be varied over a wide range, from short-

wavelength infrared (SWIR; 1-3  $\mu\text{m}$ ), the mid-infrared (MWIR; 3-5  $\mu\text{m}$ ), through long-wavelength (LWIR; 8-12  $\mu\text{m}$ ) and into the VLWIR (>12  $\mu\text{m}$ ). Unlike intrinsic detectors which utilize interband transition, quantum wells of these detectors must be doped since the photon energy is not sufficient to create photocarriers ( $h\nu < E_g$ ). It is worth noting, that various research groups have demonstrated QWIPs using other III-V material systems [2]. However, the GaAs/AlGaAs is the most commonly used material system in QWIPs due to its mature growth and processing technology [2].

## 2. N-DOPED BOUND-TO-BOUND QWIPs

The first *bound-to-bound* state QWIP was demonstrated by Levine *et al.* [4], which consisted of 50 periods of  $L_w = 65 \text{ \AA}$  GaAs quantum well and  $L_b = 95 \text{ \AA}$   $\text{Al}_{0.25}\text{Ga}_{0.75}\text{As}$  barriers sandwiched between top (0.5  $\mu\text{m}$  thick) and bottom (1  $\mu\text{m}$  thick) GaAs contact layers. The center 50  $\text{\AA}$  of the GaAs wells were doped to  $N_D = 1.4 \times 10^{18} \text{ cm}^{-3}$  and the contact layers were doped to  $N_D = 4 \times 10^{18} \text{ cm}^{-3}$ . This structure was grown by molecular beam epitaxy (MBE). These thicknesses and compositions were chosen to produce only two states in the quantum well with energy spacing give rise to a peak wavelength of 10  $\mu\text{m}$ . The measured [4] absorption spectra peaked at  $\lambda_p = 10.9 \mu\text{m}$  with a full-width at half-maximum of  $\Delta\nu = 97 \text{ cm}^{-1}$ . The peak absorbance  $a = -\log(\text{transmission}) = 2.2 \times 10^{-2}$  corresponds to a net absorption of 5% (i.e.,  $a = 600 \text{ cm}^{-1}$ ).

After the absorption of infrared photons, the photoexcited carriers can be transported either along the plane of quantum wells (with an electric field along the quantum wells) or perpendicular to the wells (with an electric field perpendicular to the epitaxial layers). As far as the infrared detection is concerned, perpendicular transport is superior to parallel transport [5] since the difference between the excited state and ground state mobilities is much larger in the latter case, and consequently, transport

perpendicular to the quantum wells (i.e., growth direction) gives a substantially high photocurrent. In addition, the heterobarriers block the transport of ground state carriers in the quantum wells, and thus lower dark current. For these reasons, QWIPs are based on escape and perpendicular transport of photoexcited carriers as shown in Fig. 2.

In the latter versions of the bound-to-bound state QWIPs, Choi *et al.* [6] has used slightly thicker and higher barriers to reduce tunneling induced dark current. When they increased the barrier thickness from  $L_b = 95 \text{ \AA}$  to  $140 \text{ \AA}$  and  $\text{Al}_x\text{Ga}_{1-x}\text{As}$  barrier height from  $x = 0.25$  to  $0.36$ , the dark current (also the photocurrent) was significantly reduced. The nonlinear behavior of the responsivity and the dark current versus bias voltage observed in the bound-to-bound QWIPs is due to the complex tunneling process associated with the high-field domain formation [6]

### **3. N-DOPED BOUND-TO-CONTINUUM QWIPs**

In the previous section, we mentioned the QWIP containing two bound states. By reducing the quantum well width, it is possible to push the strong bound-to-bound intersubband absorption into the continuum, resulting in a strong bound-to-continuum intersubband absorption. The major advantage of the bound-to-continuum QWIP is that the photoexcited electron can escape from the quantum well to the continuum transport states without tunneling through the barrier as shown in Fig. 3. As a result, the bias required to efficiently collect the photoelectrons can be reduced dramatically. Due to the fact that the photoelectrons do not have to tunnel through the barriers, the  $\text{Al}_x\text{Ga}_{1-x}\text{As}$  barrier thickness of bound-to-continuum QWIP can be increased without reducing the photoelectron collection efficiency. Increasing the barrier width from a few hundred  $\text{\AA}$  to  $500 \text{ \AA}$  can reduce the ground state sequential tunneling by an order of magnitude. By making use of these improvements, Levine *et al.* [7] has successfully demonstrated the

first bound-to-continuum QWIP with a dramatic improvement in the performance (i.e., detectivity  $3 \times 10^{10} \text{ cm}^2/\text{Hz/W}$  at 68 K for a QWIP which had cutoff wavelength at 10  $\mu\text{m}$ ).

#### **4. N-DOPED BOUND-TO-QUASIBOUND QWIPs**

Improving QWIP performance depends largely on minimizing the parasitic current (i.e., dark current) that plagues all light detectors. The dark current is the current that flows through a biased detector in the dark (i.e., with no photons impinging on it). As Gunapala and Bandara (1995) have discussed elsewhere, at temperatures above 45 K (typical for  $\lambda < 14 \mu\text{m}$ ), the dark current of the QWIP is entirely dominated by classical thermionic emission of ground state electrons directly out of the well into the energy continuum. Minimizing the dark current is critical to the commercial success of the QWIP as it allows the highly-desirable high-temperature detector operation.

Therefore, Gunapala and Bandara [2] have designed the *bound-to-quasibound* quantum well by placing the first excited state exactly at the well top as shown in Fig. 4. Dropping the first excited state to the quantum well top causes the barrier to thermionic emission (roughly the energy height from the ground state to the well top) to be  $\sim 10 \text{ meV}$  more in bound-to-quasibound QWIP than in the bound-to-continuum one, causing the dark current to drop significantly at elevated operating temperatures. The most important advantage of the bound-to-quasibound QWIP over the bound-to-continuum QWIP is that in the case of bound-to-quasibound QWIP the energy barrier for the thermionic emission is the same as it is for the photoionization as shown in Fig. 5 (Gunapala and Bandara, 1995). In the case of a bound-to-continuum QWIP the energy barrier for the thermionic emission is 10 - 15 meV less than the photoionization energy. Thus, the dark current of bound-to-quasibound QWIPs is reduced by an order of

magnitude (i.e.,  $I_d \propto e^{-\frac{\Delta E}{kT}} \approx e^{-2}$  for  $T = 55$  K) as shown in Fig. 5. In addition, when the first excited state resonate with the quantum well barrier top (i.e., quasibound QWIP), the intersubband absorption process goes through a resonance [9]. Thus, the optical absorption of the bound-to-quasibound QWIP is significantly higher than the bound-to-continuum QWIP.

## 5. COMPARISON OF BOUND, QUASIBOUND, AND CONTINUUM QWIPs

Now we will discuss and compare the optical and transport properties of bound-to-continuum QWIPs, bound-to-bound QWIPs, and bound-to-quasibound QWIPs with each other. The structures of the six samples to be discussed are listed in Table I. These n-doped QWIPs were grown using MBE and the wells and contact layers were doped with Si. The quantum well widths  $L_w$  range from 40 Å to 70 Å, while the barrier widths are approximately constant at  $L_b = 500$  Å. The Al molar fraction, in the  $Al_xGa_{1-x}As$  barriers, varies from  $x = 0.10$  to 0.31 (corresponding to cutoff wavelengths of  $\lambda_c = 7.9 - 19$  μm). The photosensitive doped MQW region containing 25 to 50 periods is sandwiched between similarly doped top (0.5 μm) and bottom (1 μm) ohmic contact layers. These structural parameters have been chosen to give a very wide variation in QWIP absorption and transport properties [10]. In particular, samples A through D are n-doped with intersubband infrared transition occurring between a single localized bound state in the well and a delocalized state in the continuum (denoted B-C in Table I) [7,11-18]. Sample E has a high Al concentration  $x = 0.26$  coupled with a wide well  $L_w = 50$  Å, yielding two bound states in the well. Thus, the intersubband transition from the bound ground state to the bound first excited state, (denoted B-B in Table I), and therefore requires electric field assisted tunneling for the photoexcited carrier to escape into the continuum as discussed in the previous section [4,19,20]. Sample F was designed to have a quasibound excited state (denoted B-QB in Table I) [2], which is intermediate between a

strongly bound excited state and weakly bound continuum state. It consists of a  $L_w = 45$  Å doped quantum well and 500 Å of a  $\text{Al}_x\text{Ga}_{1-x}\text{As}$  barrier with  $x = 0.3$ . These quantum well parameters result in a first excited state in resonance with the barriers, and is thus expected to have an intermediate behavior.

### 5.1 ABSORPTION SPECTRA

The infrared absorption spectra for samples A-F were measured at room temperature, using a 45° multipass waveguide geometry (except for sample D which was at such a long-wavelength, that the substrate multiphonon absorption obscured the intersubband transition). As can be readily seen in Fig. 6, the spectra of the bound-to-continuum QWIPs (samples A, B, and C) are much broader than the bound-to-bound or bound-to-quasibound QWIPs (samples E and F or the QWIPs discussed in the previous section). Correspondingly, the magnitude of the absorption coefficient  $\alpha$  for the continuum QWIPs (left-hand scale) is significantly lower than that of the bound-to-bound QWIPs (right-hand scale), due to the conservation of oscillator strength. That is,  $\alpha_p(\Delta\lambda/\lambda)/N_D$  is a constant, as was previously found [21]. The values of the peak room temperature absorption  $\alpha_p$ , peak wavelength  $\lambda_p$ , cutoff wavelength  $\lambda_c$  (long wavelength  $\lambda$  for which  $\alpha$  drops to half- $\alpha_p$ ) and spectral width  $\Delta\lambda$  (full width at half  $\alpha_p$ ) are given in Table II. The room temperature absorption quantum efficiency  $\eta_a(300\text{ K})$  evaluated from  $\alpha_p(300\text{ K})$  using

$$\eta_a = \frac{1}{2}(1 - e^{-2\alpha_p \ell}) \quad (3)$$

where  $\eta_a$  is the unpolarized double-pass absorption quantum efficiency, where  $\ell$  is the length of the photosensitive region, and the factor of two in the denominator is a result of the quantum mechanical selection rules, which only allows the absorption of radiation

polarized in the growth direction. The low temperature quantum efficiency  $\eta_a(77)$  was obtained by using  $\alpha_p(77 \text{ K}) \approx 1.3 \alpha_p(300 \text{ K})$  as previously discussed. The last column containing  $\eta_{\max}$  will be discussed later.

In order to clearly compare the line shapes of the bound, quasibound, and continuum QWIPs, the absorption coefficients for samples A, E, and F have been normalized to unity and plotted as  $\tilde{\alpha}$  in Fig. 7, and the wavelength scale has been normalized by plotting the spectra against  $\Delta\lambda \equiv (\lambda - \lambda_p)$ , where  $\lambda_p$  is the wavelength at the absorption peak. The very large difference in spectral width is apparent with the bound and continuum excited state transitions ( $\Delta\lambda/\lambda = 9\%-11\%$ ) being 3-4 times narrower than for the continuum excited state QWIPs ( $\Delta\lambda/\lambda = 33\%$ ).

## 5.2 DARK CURRENT

In order to measure the dark current-voltage curves, 200  $\mu\text{m}$  diam mesas were fabricated as described elsewhere [2] and the results are shown in Fig. 8 for  $T = 77 \text{ K}$ . Note that the asymmetry in the dark current [22] with  $I_d$  being larger for positive bias (i.e., mesa top positive) than for negative bias. This can be attributed to the dopant migration in the growth direction [23], which lowers the barrier height of the quantum wells in the growth direction compared to the quantum well barriers in the other direction (which are unaffected). Note that, as expected, the dark current  $I_d$  increases as the cutoff wavelength  $\lambda_c$  increases. At bias  $V_b = -1\text{V}$  and  $1\text{V}$ , the curves for samples E and F cross. This is due to the fact that even though sample E has a shorter cutoff wavelength than sample F, it is easy for the excited electrons to tunnel out at sufficiently high bias. In contrast, sample F has a quasibound excited state, which is in resonance with the  $L_b = 500 \text{ \AA}$  thick barrier top.

Levine *et al.* [7] has analyzed the origin of the dark current in detail and shown that thermionic-assisted tunneling is a major source of dark current [14,21,22,24,25]. In that analysis, they first determine the effective number of electrons  $n(V)$ , which are thermally excited out of the well into the continuum transport states, as a function of bias voltage  $V$ ;

$$n(V) = \left( \frac{m^*}{\pi \hbar^2 L_p} \right) \int_{E_0}^{\infty} f(E) T(E, V) dE \quad (4)$$

where the first factor containing the effective mass  $m^*$  is obtained by dividing the two-dimensional density of states by the superlattice period  $L_p$  (to convert it into an average three-dimensional density), and where  $f(E)$  is the Fermi factor  $f(E) = [1 + \exp((E - E_0 - E_F)/kT)]^{-1}$ ,  $E_0$  is the ground state energy,  $E_F$  is the two-dimensional Fermi level, and  $T(E, V)$  is the bias-dependent tunneling current transmission factor for a single barrier which can be calculated using Wentzel-Kramers-Brillouin (WKB) approximation to a biased quantum well. Equation (4) accounts for both thermionic emission above the energy barrier  $E_b$  (for  $E > E_b$ ) and thermionically assisted tunneling (for  $E < E_b$ ). Then they calculated the bias dependent dark current  $I_d(V)$  using  $I_d(V) = n(V)ev(V)A$ , where  $e$  is the electronic charge,  $A$  is the area of the detector, and  $v$  is the average transport velocity given by

$$v(V) = \mu F [1 + (\mu F / v_s)^2]^{-\frac{1}{2}} \quad (5)$$

where  $\mu$  is the mobility,  $F$  is the average electric field, and  $v_s$  is the saturated drift velocity. The good agreement is achieved as a function of both bias voltage and temperature over a range of eight orders of magnitude in dark current [7].

### 5.3 RESPONSIVITY

The responsivity spectra  $R(\lambda)$  were measured on 200  $\mu\text{m}$  diam. mesa detectors using a polished  $45^\circ$  incident facet on the detector, together with a globar source and a monochromator [22]. A dual lock-in ratio system with a spectrally flat pyroelectric detector was used to normalize the system spectral response due to wavelength dependence of the blackbody, spectrometer, filters, etc. The absolute magnitude of the responsivity was accurately determined by measuring the photocurrent  $I_p$  with a calibrated blackbody source. This photocurrent is given by

$$I_p = \int_{\lambda_1}^{\lambda_2} R(\lambda)P(\lambda)d\lambda \quad (6)$$

where  $\lambda_1$  and  $\lambda_2$  are the integration limits that extend over the responsivity spectrum, and  $P(\lambda)$  is the blackbody power per unit wavelength incident on the detector, which is given by

$$P(\lambda) = W(\lambda)\sin^2(\theta/2)AF\cos\phi \quad (7)$$

where  $A$  is the detector area,  $\phi$  is the angle of incidence,  $\theta$  is the optical field of view angle (i.e.,  $\sin^2(\theta/2) = (4f^2+1)^{-1}$  where  $f$  is the  $f$  number of the optical system; in this case  $\theta$  is defined by the radius  $\rho$  of the blackbody opening at a distance  $D$  from the detector, so that  $\tan(\theta/2) = \rho/D$ ),  $F$  represents all coupling factors and  $F = T_f(1-r)C$  where  $T_f$  is the transmission of filters and windows,  $r = 28\%$  is the reflectivity of the GaAs detector surface,  $C$  is the optical beam chopper factor ( $C = 0.5$  in an ideal optical beam chopper), and  $W(\lambda)$  is the blackbody spectral density given by the following equation (i.e., the power radiated per unit wavelength interval at wavelength  $\lambda$  by a unit area of a blackbody at temperature  $T_B$ ).

$$W(\lambda) = (2\pi c^2 h / \lambda^5) (e^{hc/\lambda k T_B} - 1)^{-1} \quad (8)$$

By combining equations(6) and (7), and using  $R(\lambda) = R_p \tilde{R}(\lambda)$ , where  $R_p$  is the peak responsivity and  $\tilde{R}(\lambda)$  is normalized (at peak wavelength  $\lambda_p$ ) experimental spectral responsivity, we can rewrite the photocurrent  $I_p$  as

$$I_p = R_p G \int_{\lambda_1}^{\lambda_2} \tilde{R}(\lambda) W(\lambda) d\lambda \quad (9)$$

where  $G$  represents all the coupling factors and is given by  $G = \sin^2(\theta/2) A F \cos \phi$ . Thus, by measuring the  $T_B = 1000$  K blackbody photocurrent,  $R_p$  can be accurately determined.

The normalized responsivity spectra  $\tilde{R}(\lambda)$  are given in Fig. 9 for samples A-F, where we again see that the bound and quasibound excited state QWIPs (samples E and F) are much narrower  $\Delta\lambda/\lambda = 10\%-12\%$  than the continuum QWIPs  $\Delta\lambda/\lambda = 19\%-28\%$  (samples A-D). Table III gives the responsivity peak  $\lambda_p$  and cutoff wavelengths  $\lambda_c$  as well as the responsivity spectral width  $\Delta\lambda$ . These responsivity spectral parameters are given in Table III and are similar to the corresponding absorption values listed in Table II.

The absolute peak responsivity  $R_p$  can be written in terms of quantum efficiency  $\eta$  and photoconductive gain  $g$  as

$$R_p = (e/h\nu) \eta g. \quad (10)$$

Responsivity versus bias voltage curves for the bound, quasibound, and continuum, samples are shown in Fig. 10. Note that, at low bias, the responsivity is nearly linearly dependent on bias and it saturates at high bias. This saturation occurs due

to the saturation of drift velocity. For the longest wavelength sample D, where  $\lambda_c = 19 \mu\text{m}$ , the dark current becomes too large at high bias to observe the saturation in  $R_p$ . The quasibound QWIP (sample F) behaves quite similarly to the bound QWIPs. The fully bound sample E has a significantly lower responsivity. The responsivity does not start out linearly with bias but is in fact zero for finite bias. That is, there is a zero bias offset, due to the necessity of field assisted tunneling for the photoexcited carrier to escape from the well [4,20,26]

#### 5.4 DARK CURRENT NOISE

The dark current noise  $i_n$  was measured on a spectrum analyzer for all of the samples at  $T = 77 \text{ K}$  as a function of bias voltage [22]. The result for sample B is shown in Fig. 11. The solid circles were measured for negative bias (mesa top negative) while the open circles are for positive bias. The smooth curves are drawn through the experimental data. Note that the current shot noise for positive bias is much larger than that for negative bias (e.g., at  $V_b = 3.5 \text{ V}$ , it is 4 times larger). Also that near  $V_b = 4 \text{ V}$  there is a sudden increase in the noise due to a different mechanism (possibly due to the avalanche gain [27] process). This asymmetry in the dark current noise is due to the previously mentioned asymmetry in  $I_d$ . The photoconductive gain  $g \sim g_n$  (for low capture probabilities) can now be obtained using the current shot noise expression [7,28-31]

$$i_n = \sqrt{4eI_d g_n \Delta f}, \quad (11)$$

where  $\Delta f$  is the band width, (taken as  $\Delta f = 1 \text{ Hz}$ ). The photoconductive gain of QWIPs can be written as [30,31]

$$g = L/\ell, \quad (14)$$

where  $L$  is the hot carrier mean free path and  $\ell$  is the superlattice length ( $\ell = 2.7 \mu\text{m}$  for sample B).

The photoconductive gain of a typical 50 well QWIP structure, increases approximately linearly with the bias at low voltage and saturates near  $g \sim 0.3$  at high voltages ( $V_b > 3 \text{ V}$ , due to velocity saturation. However, the large difference in responsivities of the bound-to-continuum, bound-to-quasibound and bound-to-bound QWIPs are associated with the transmission factor,  $\gamma$  which is defined as the fraction of carriers which escape from the excited state of the well and enter the continuum [31]. It is worth noting that, this transmission factor is a strongly depends on the bias as well as the position of the excited state with respect to the barrier top. Typically,  $\gamma$  of bound-to-continuum detectors is larger than  $\gamma$  of bound-to-bound detectors, and has a weaker bias voltage dependence. This is to be expected since the photoexcited carriers in bound-to-continuum QWIPs are above the top of the barriers and, thus, readily escape before being recaptured. However, the bound-to-bound QWIP is quite different due to the necessity of field assisted tunneling in order for excited photoelectrons to escape from the quantum well [10,31].

### 5.5 DETECTIVITY

We can now determine the peak detectivity  $D_\lambda^*$  defined as [7,22]

$$D_\lambda^* = R_p^0 \frac{\sqrt{A\Delta f}}{i_n} \quad (15)$$

where  $A$  is the detector area and  $\Delta f = 1 \text{ Hz}$ . This is done as a function of bias for a continuum (A), a bound (E), and a quasibound (F) QWIP in Fig. 12. (The dashed lines

near the origin are extrapolations.) For all three samples  $D^*$  has a maximum value at a bias between  $V_b = -2$  and  $-3$  V. Since these QWIPs all have different cutoff wavelengths, these maximum  $D^*$  values cannot be simply compared. However, this analysis clearly compare the absorption, responsivity, spectral shape, and dark current of bound-to-bound, bound-to-continuum, and bound-to-quasibound QWIPs. In order to facilitate this comparison, we note that the dark current has been demonstrated to follow an exponential law [7,22]  $I_d \propto e^{-(E_c - E_f)/kT}$  (where  $E_c$  is the cutoff energy  $E_c = hc / \lambda_c$ ) over a wide range of both temperature and cutoff wavelength. Thus using  $D^* \propto (R_p / i_n)$ , we have

$$D^* = D_0^\lambda e^{E_c/2kT} \quad (16)$$

In order to compare the performance of these different QWIPs Levine *et al.* [10] have plotted  $D^*$  against  $E_c$  on a log scale [7,22,33]. The straight line fit the data very well which is satisfying considering the samples have different doping densities,  $N_d$ , different methods of crystal growth, different spectral widths  $\Delta\lambda$ , different excited states (bound, quasibound, and continuum) and even, in one case, a different materials system (InGaAs/InP) [33]. The best fit for  $T = 77$  K detectivities of n-doped QWIPs is

$$D_c^* = 1.1 \times 10^6 e^{E_c/2kT} \text{ cm}\sqrt{\text{Hz}} / \text{W} \quad (21)$$

Since QWIP dark current is mostly due to thermionic emission and thermionically assisted tunneling, unlike other detectors, QWIP detectivity increases nearly exponentially with the decreasing temperature.

## **6. SUMMARY**

The performance of GaAs/AlGaAs based bound-to-bound, bound-to-continuum, and bound-to-quasibound QWIPs were compared. This discussion, clearly shows the importance of the position of first excited state in the quantum wells of QWIPs. Our discussion of QWIPs has been necessarily brief and the literature references cited are not all inclusive, but represent a selection of key articles from a historic and technical point of view. Exceptionally rapid progress has been made in the performance of long-wavelength QWIP FPAs [34-36].

## **ACKNOWLEDGMENTS**

The QWIP research described in this paper was performed partly by the Center for Space Microelectronics Technology, Jet Propulsion Laboratory, California Institute of Technology, and were jointly sponsored by the Ballistic Missile Defense Organization / Innovative Science & Technology Office, the National Aeronautics and Space Administration, Office of Space Science, and Air Force Research Laboratory.

### **REFERENCES**

1. C. Weisbuch, *Semiconductor and Semimetals* **24**, 1(1987).
2. S. D. Gunapala and K. M. S. V. Bandara, *Physics of Thin Films*, Academic Press **21**, 113 (1995).
3. B. F. Levine, *J. Appl. Phys.* **74**, R1 (1993).
4. B. F. Levine, K. K. Choi, C. G. Bethea, J. Walker, and R. J. Malik, *Appl. Phys. Lett.*, **50**, 1092 (1987).
5. R. G. Wheeler and H. S. Goldberg, *IEEE Trans. Electron Devices* **ED-22**, 1001 (1975).
6. K. K. Choi, B. F. Levine, N. Jarosik, J. Walker, and R. J. Malik, *Appl. Phys. Lett.*, **50**, 1814 (1987).
7. B. F. Levine, C. G. Bethea, G. Hasnain, V. O. Shen, E. Pelve, R. R. Abbott, and S. J. Hsieh, *Appl. Phys. Lett.*, **56**, 851 (1990).
8. B. F. Levine, C. G. Bethea, G. Hasnain, J. Walker, and R. J. Malik, *Appl. Phys. Lett.*, **53**, 296 (1988).
9. D. D. Coon, R. P. G. Karunasiri, *Appl. Phys. Lett.*, **45**, 649 (1984).
10. B. F. Levine, A. Zussman, S. D. Gunapala, M. T. Asom, J. M. Kuo, and W. S. Hobson, *J. Appl. Phys.* **72**, 4429, (1992).
11. B. F. Levine, C. G. Bethea, K. K. Choi, J. Walker, and R. J. Malik, *J. Appl. Phys.* **64**, 1591 (1987).
12. B. F. Levine, S. D. Gunapala, and M. Hong, *Appl. Phys. Lett.* **59**, 1969 (1991).
13. J. Y. Andersson and L. Lundqvist, *Appl. Phys. Lett.* **59**, 857 (1991).
14. S. R. Andrews and B. A. Miller, *J. Appl. Phys.* **70**, 993 (1991).
15. B. K. Janousek, M. J. Daugherty, W. L. Bloss, M. L. Rosenbluth, M. J. O'Loughlin, H. Kanter, F. J. De Luccia, and L. E. Perry, *J. Appl. Phys.* **67**, 7608 (1990).

16. M. J. Kane, M. T. Emeny, N. Apsley, and C. R. Whitehouse, *Electron. Lett.* **25**, 230 (1989).
17. A. G. Steele, H. C. Liu, M. Buchanan, and Z. R. Wasilewski, *Appl. Phys. Lett.* **59**, 3625 (1991).
18. C. S. Wu, C. P. Wen, R. N. Sato, M. Hu, C. W. Tu, J. Zhang, L. D. Flesner, L. Pham, and P. S. Nayer, *IEEE Trans. Electron Devices* **39**, 234 (1992).
19. B. F. Levine, G. Hasnain, C. G. Bethea, and N. Chand, *Appl. Phys. Lett.* **54**, 2704 (1989).
20. K. K. Choi, B. F. Levine, C. G. Bethea, J. Walker, R. J. and Malik, *Phys. Rev. Lett.*, **59**, 2459 (1987).
21. S. D. Gunapala, B. F. Levine, L. Pfeiffer, and K. West, *J. Appl. Phys.* **69**, 6517 (1990).
22. A. Zussman, B. F. Levine, J. M. Kuo, and J. de Jong, *J. Appl. Phys.* **70**, 5101 (1991).
23. H. C. Liu, Z. R. Wasilewski, M. Buchanan, *Appl. Phys. Lett.* **63**, 761 (1993).
24. M. A. Kinch and A. Yariv, *Appl. Phys. Lett.* **55**, 2093 (1989).
25. E. Pelve, F. Beltram, C. G. Bethea, B. F. Levine, V. O. Shen, S. J. Hsieh, and R. R. Abbott, *J. Appl. Phys.* **66**, 5656 , (1989).
26. N. Vodjdani, B. Vinter, V. Berger, E. Bockenhoff, and E. Costard, *Appl. Phys. Lett.* **59**, 555 (1991).
27. B. F. Levine, K. K. Choi, C. G. Bethea, J. Walker, and R. J. Malik, *Appl. Phys. Lett.*, **51**, 934 (1987).
28. H. C. Liu, *Appl. Phys. Lett.* **60**, 1507 (1992).
29. W. A. Beck, *Appl. Phys. Lett.* **63**, 3589 (1993).
30. G. Hasnain, B. F. Levine, S. D. Gunapala, and N. Chand, *Appl. Phys. Lett.* **57**, 608 (1990).
31. K. K. Choi, *J. Appl. Phys.*, **80**, 1257 (1996).

32. A. Kastalsky, T. Duffield, S. J. Allen, and J. Harbison, *Appl. Phys. Lett.* **52**, 1320 (1988).
33. S. D. Gunapala, B. F. Levine, D. Ritter, R. A. Hamm, and M. B. Panish, *Appl. Phys. Lett.* **58**, 2024 (1991).
34. S. D. Gunapala, J. S. Park, G. Sarusi, T. L. Lin, J. K. Liu, P. D. Maker, R. E. Muller, C. A. Shott, T. Hoelter, and B. F. Levine, *IEEE Trans. Electron Devices* **44**, 45 (1997).
35. S. D. Gunapala, J. K. Liu, J. S. Park, M. Sundaram, C. A. Shott, T. Hoelter, T. L. Lin, S. T. Massie, P. D. Maker, R. E. Muller, and G. Sarusi, *IEEE Trans. Electron Devices* **44**, 51 (1997).
36. S. D. Gunapala, S. V. Bandara, J. K. Liu, W. Hong, M. Sundaram, P. D. Maker, R. E. Muller, C. A. Shott, and R. Carralejo, *IEEE Trans. Electron Devices* **45**, 1890 (1998).

### **FIGURE CAPTIONS**

- Fig. 1 Schematic band diagram of a quantum well. Intersubband absorption can take place between the energy levels of a quantum well associated with the conduction band (n-doped) or the valence band (p-doped). [2]
- Fig. 2 Conduction-band diagram for a bound-to-bound QWIP, showing the photoexcitation (intersubband transition) and tunneling out of well. [7]
- Fig. 3 Conduction-band diagram for a bound-to-continuum QWIP, showing the photoexcitation and hot-electron transport process. [8]
- Fig. 4 Schematic diagram of the conduction band in a bound-to-quasibound QWIP in an externally applied electric field. Absorption of infrared photons can photoexcite electrons from the ground state of the quantum well into the continuum, causing a photocurrent. Three dark current mechanisms are also shown: ground state tunneling (1); thermally assisted tunneling (2); and thermionic emission (3). The inset shows a cross-section transmission electron micrograph of a QWIP sample. [34]
- Fig. 5 Comparison of dark currents of bound-to-continuum and bound-to-quasibound VLWIR QWIPs as a function of bias voltage at temperature  $T = 55$  K. [2]
- Fig. 6 Absorption coefficient spectra Vs wavelength measured at  $T=300$  K for samples A, B, C, E, and F. [3,34]

Fig. 7 Normalized absorption spectra Vs wavelength difference  $\Delta\lambda=(\lambda-\lambda_p)$ . The spectral width  $\Delta\lambda/\lambda$  are also given. The insert show the schematic conduction band diagram for sample A (bound-to-continuum), sample E (bound-to-bound), and sample F (*bound-to-quasibound*). [3,34]

Fig. 8 Dark current  $I_d$  as a function of bias voltage  $V_b$  at  $T=77$  K for samples A-F. [3,34]

Fig. 9 Normalized responsivity spectra Vs wavelength measured at  $T=20$  K for samples A-F. [3,34]

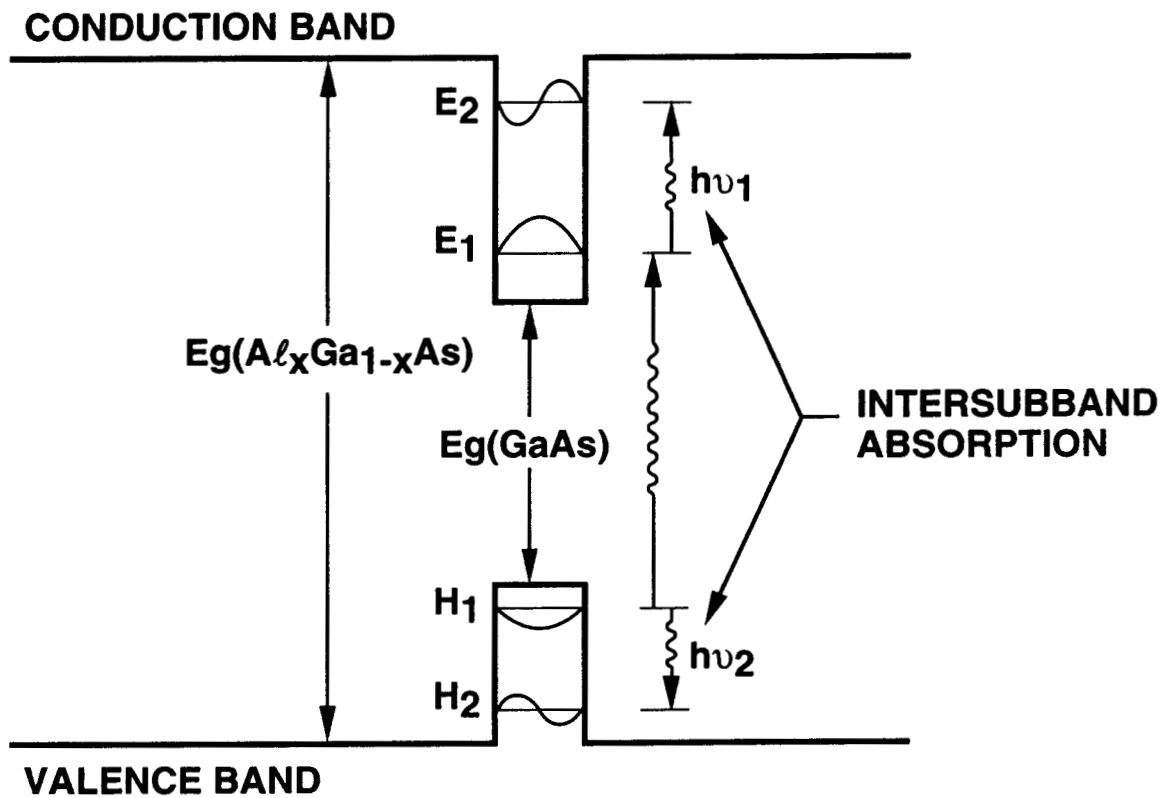
Fig. 10 Bias dependent peak ( $\lambda = \lambda_p$ ) responsivity  $R_p^0$  measured at  $T=20$  K for samples A-F. The inserts show the conduction band diagrams. [3,34]

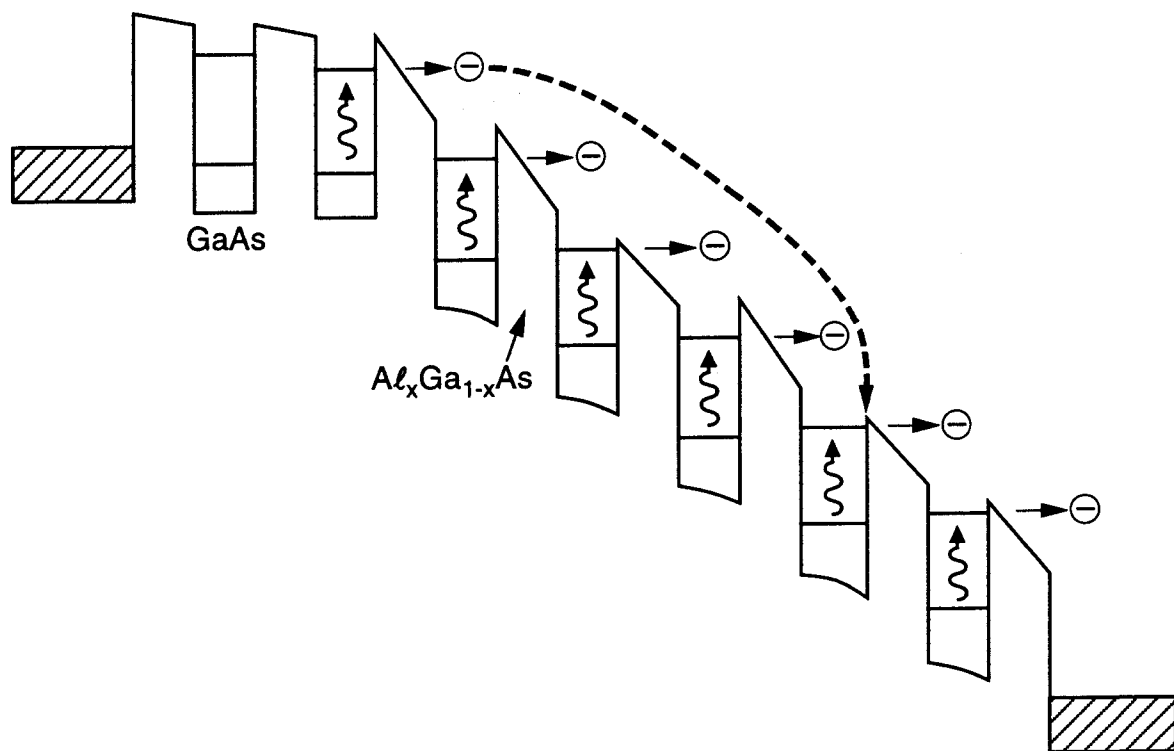
Fig. 11 Dark current noise  $i_n$  (at  $T=77$  K) Vs bias voltage  $V_b$  for sample B. Both positive (open circles) and negative (solid circles) bias are shown. The smooth curves are drawn through the measured data. The insert shows the conduction band diagram. [3]

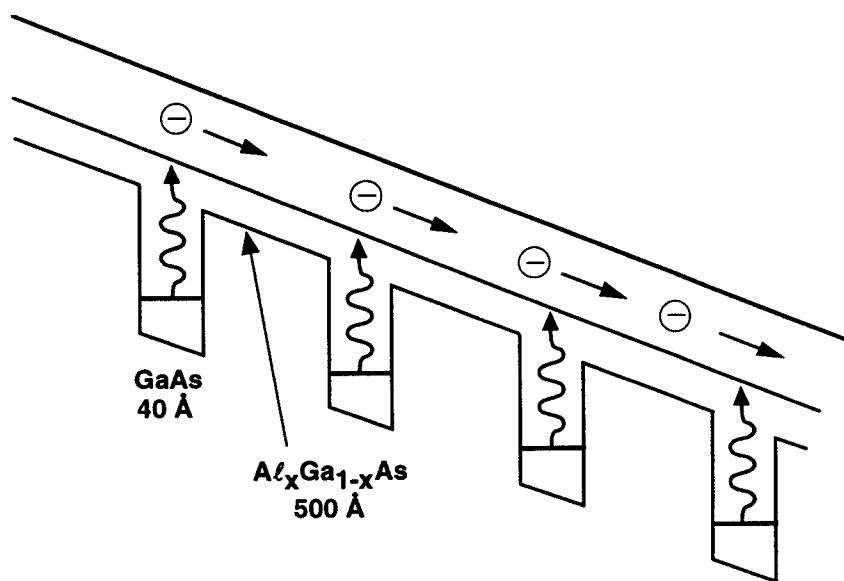
Fig. 12 Detectivity  $D^*$  (at  $T=77$  K) Vs bias voltage  $V_b$  for samples A, E and F. The inserts show the conduction band diagram. [3,34]

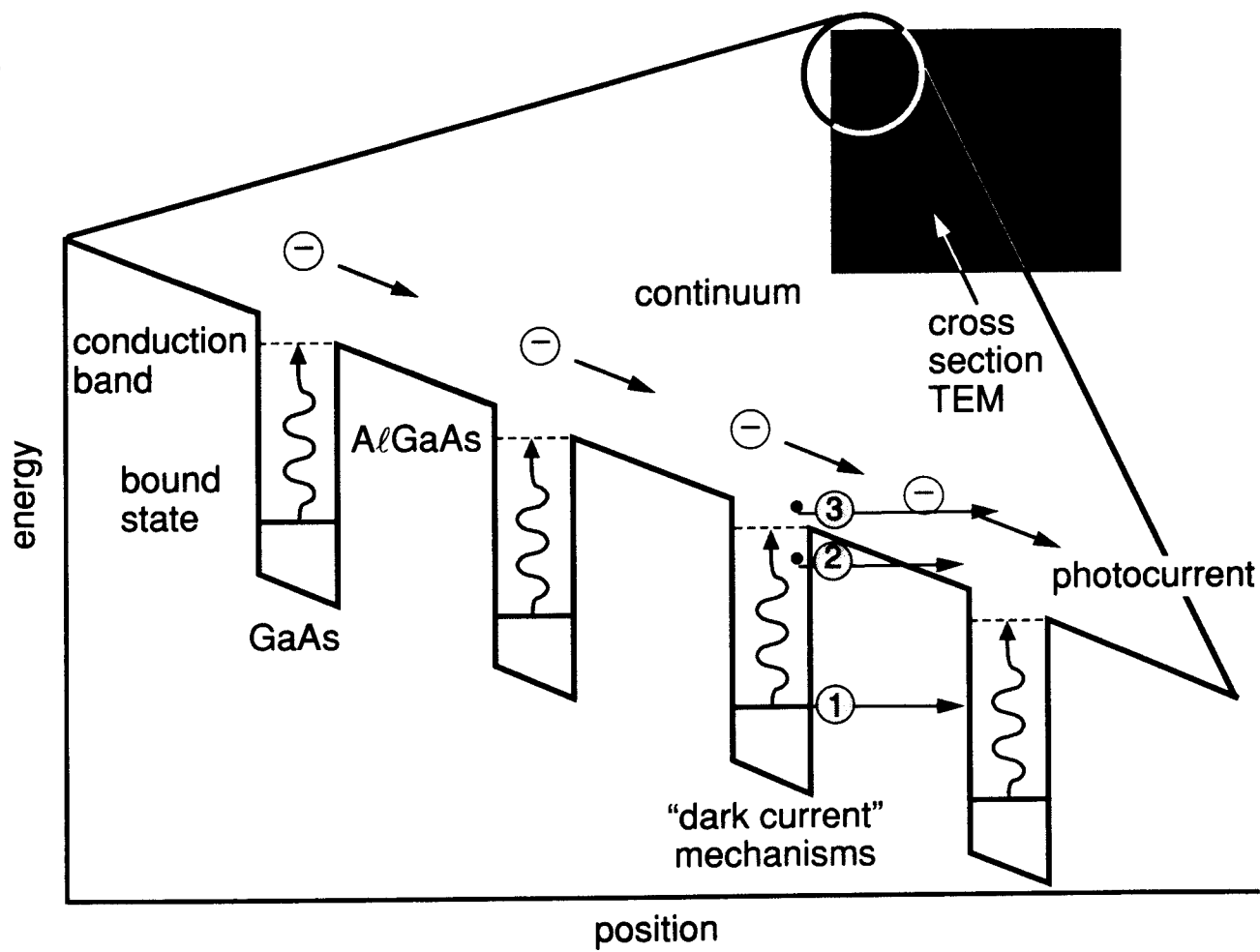
## **TABLES**

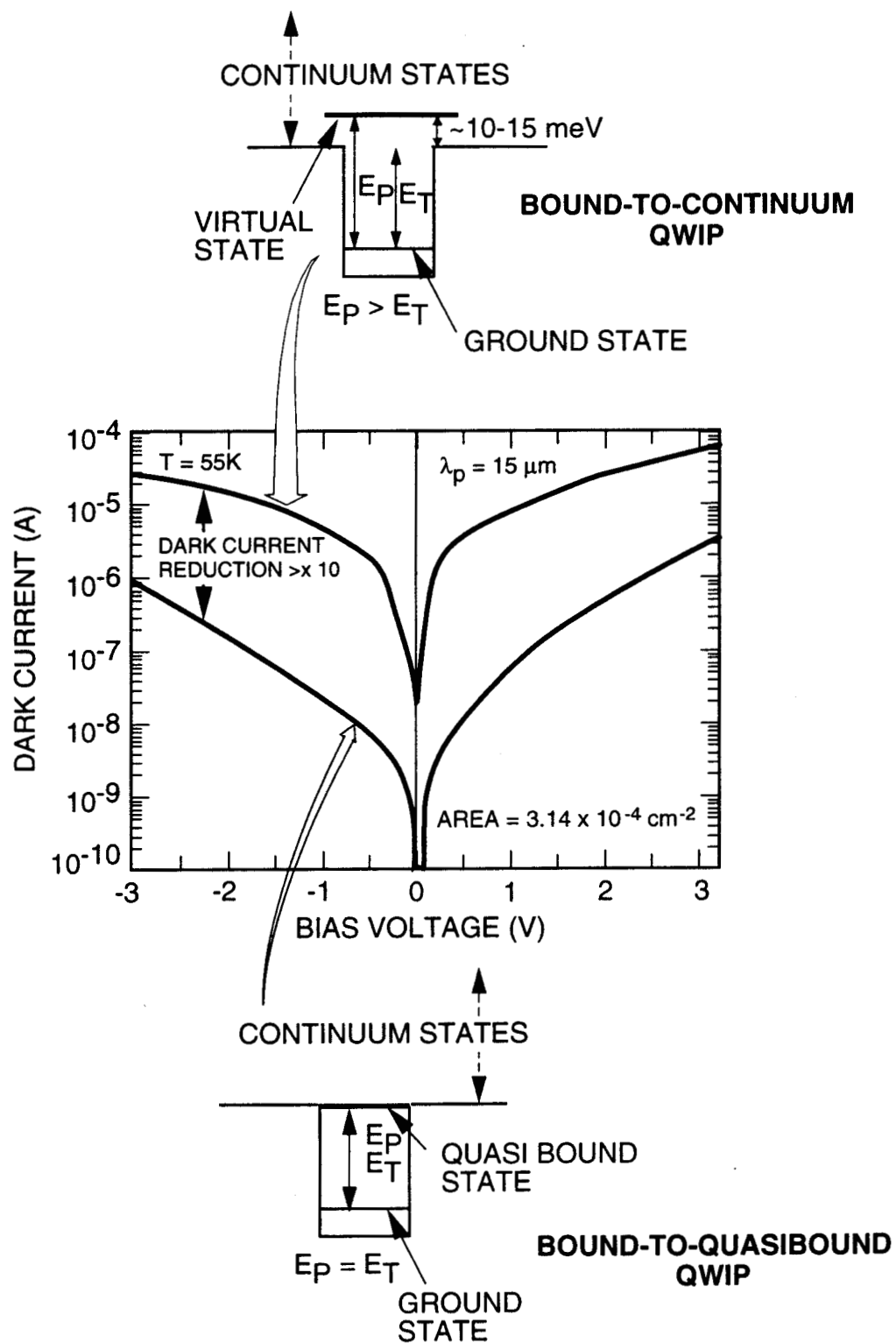
- I. Structure parameters for samples A-F, including quantum well width  $L_w$ , barrier width  $L_b$ ,  $Al_xGa_{1-x}As$  composition  $x$ , doping density  $N_D$ , doping type, number of MQW periods, and type of intersubband transition *bound-to-continuum* (B-C), *bound-to-bound* (B-B), and *bound-to-quasibound* (B-QB). [10,34]
  
- II. Optical absorption parameters for samples A, B, C, E, and F, including peak absorption wavelength  $\lambda_p$ , long wavelength cutoff  $\lambda_c$ , spectral width  $\Delta\lambda$ , fractional spectral width  $\Delta\lambda/\lambda$ , peak room temperature absorption coefficient  $\alpha_p$  (300 K), peak room temperature absorption quantum efficiency  $\eta_a$  (300 K),  $T = 77$  K absorption quantum efficiency  $\eta_a$  (77 K), and maximum high bias net quantum efficiency  $\eta_{max}$ . [10,34]
  
- III. Responsivity spectral parameter for samples A-F, including peak responsivity wavelength  $\lambda_p$ , long wavelength cutoff  $\lambda_c$ , spectral width  $\Delta\lambda$ , and fractional spectral width  $\Delta\lambda/\lambda$ . [10,34]

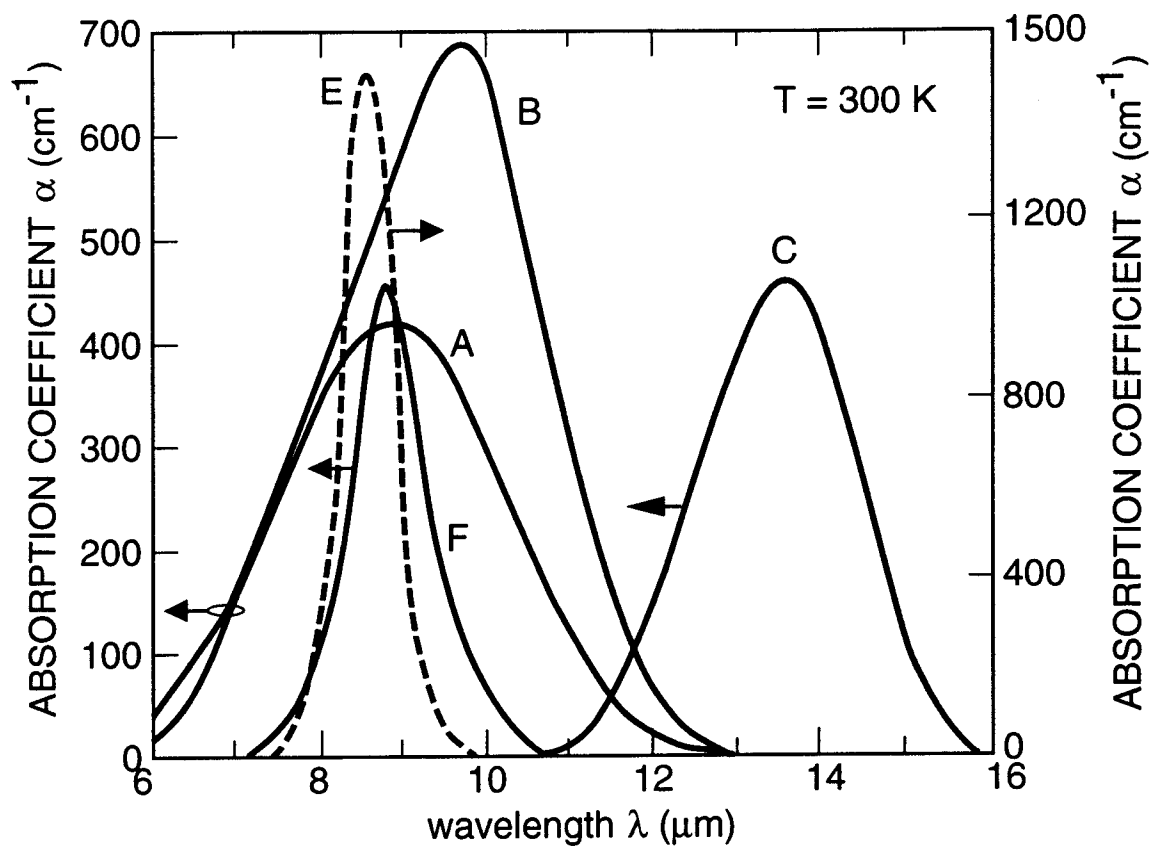


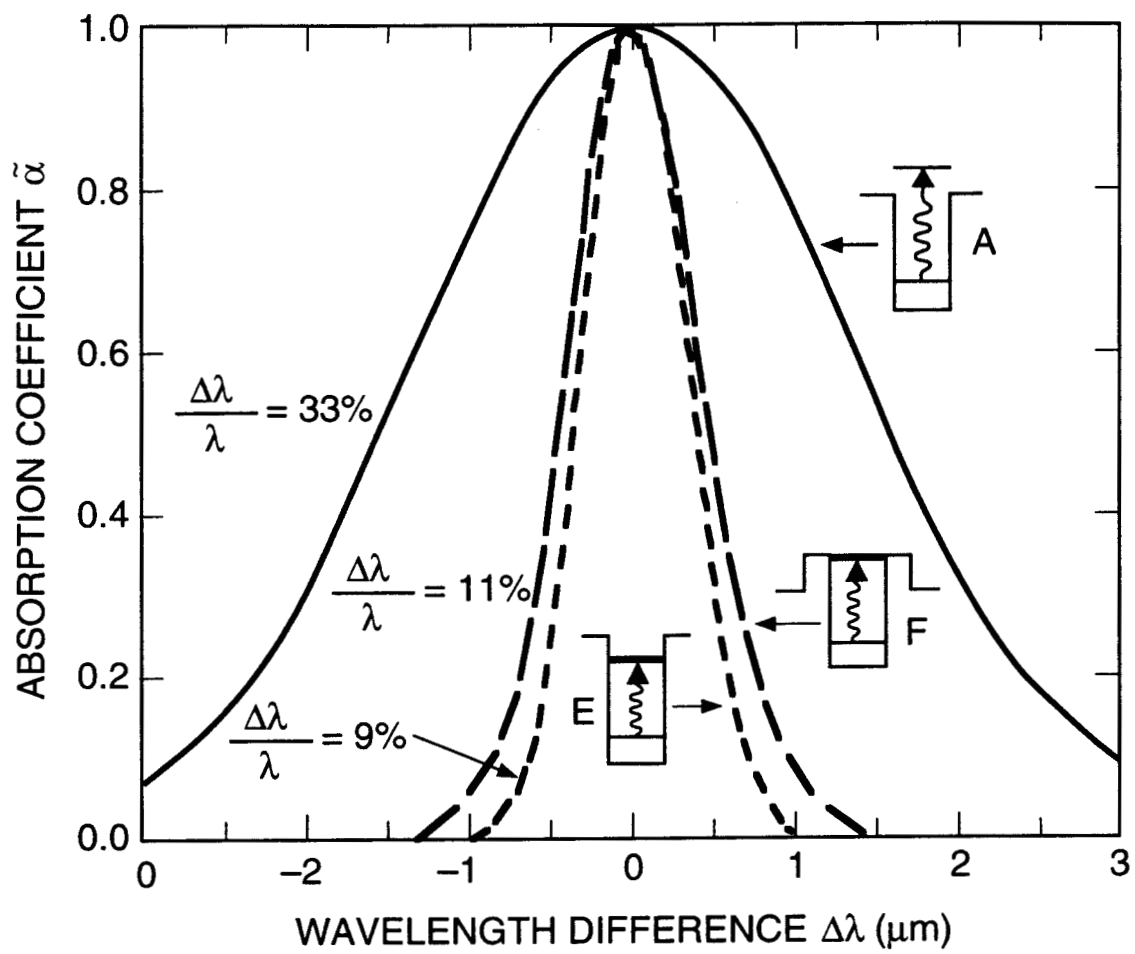


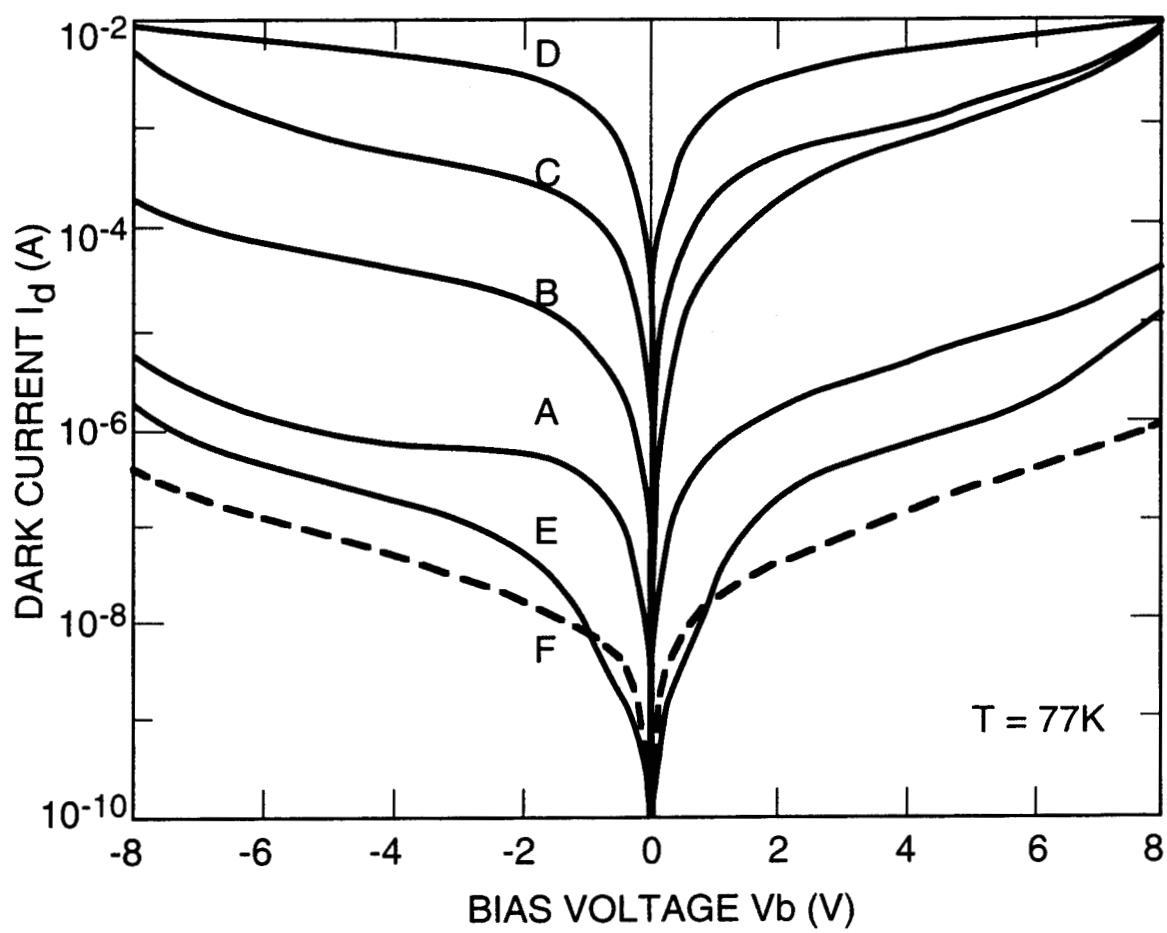


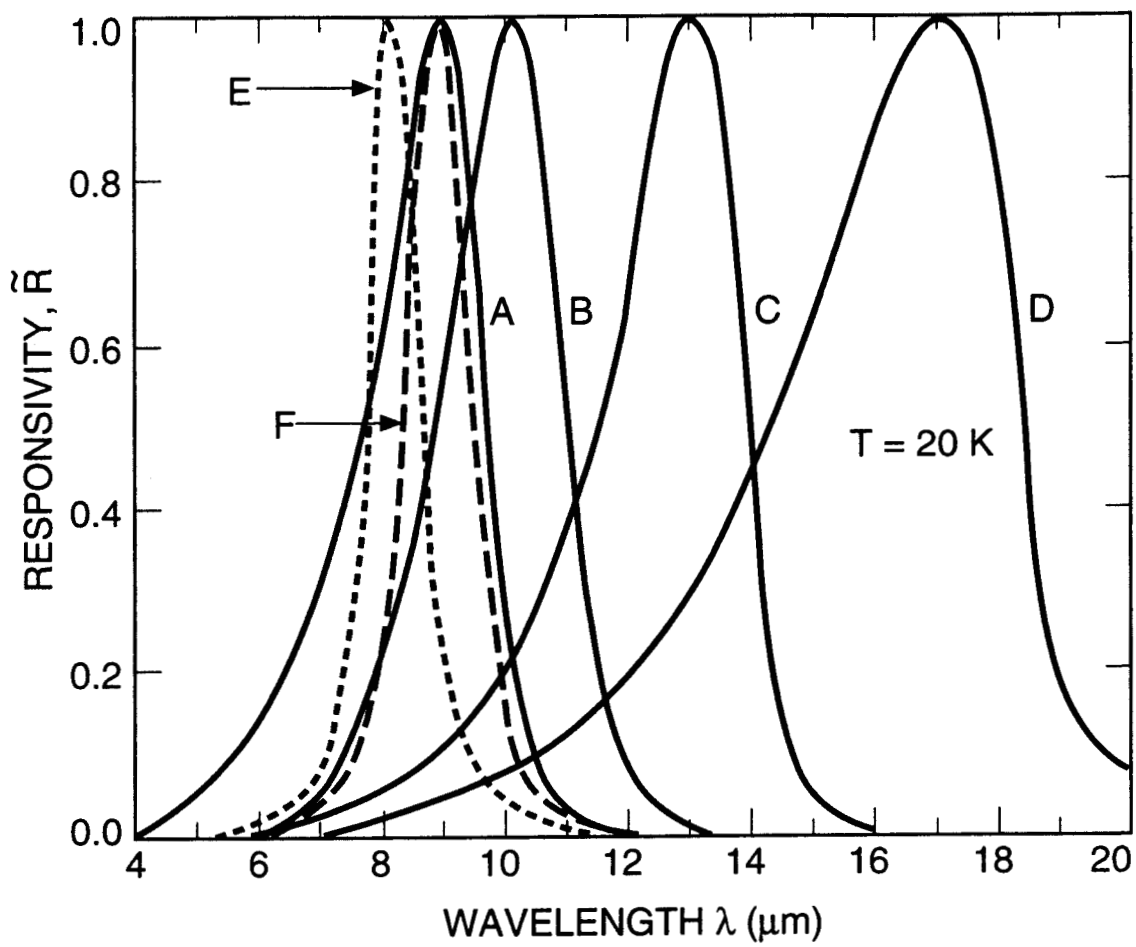


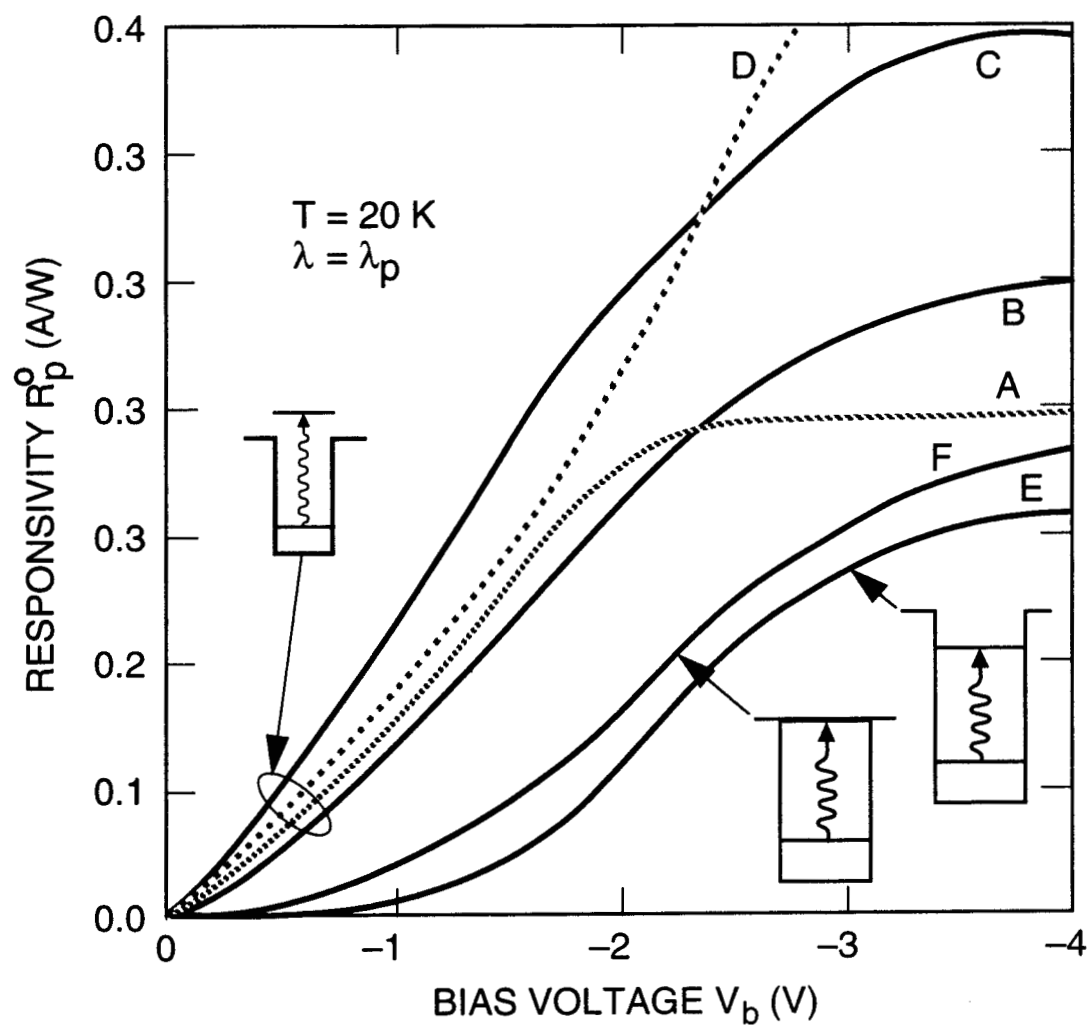


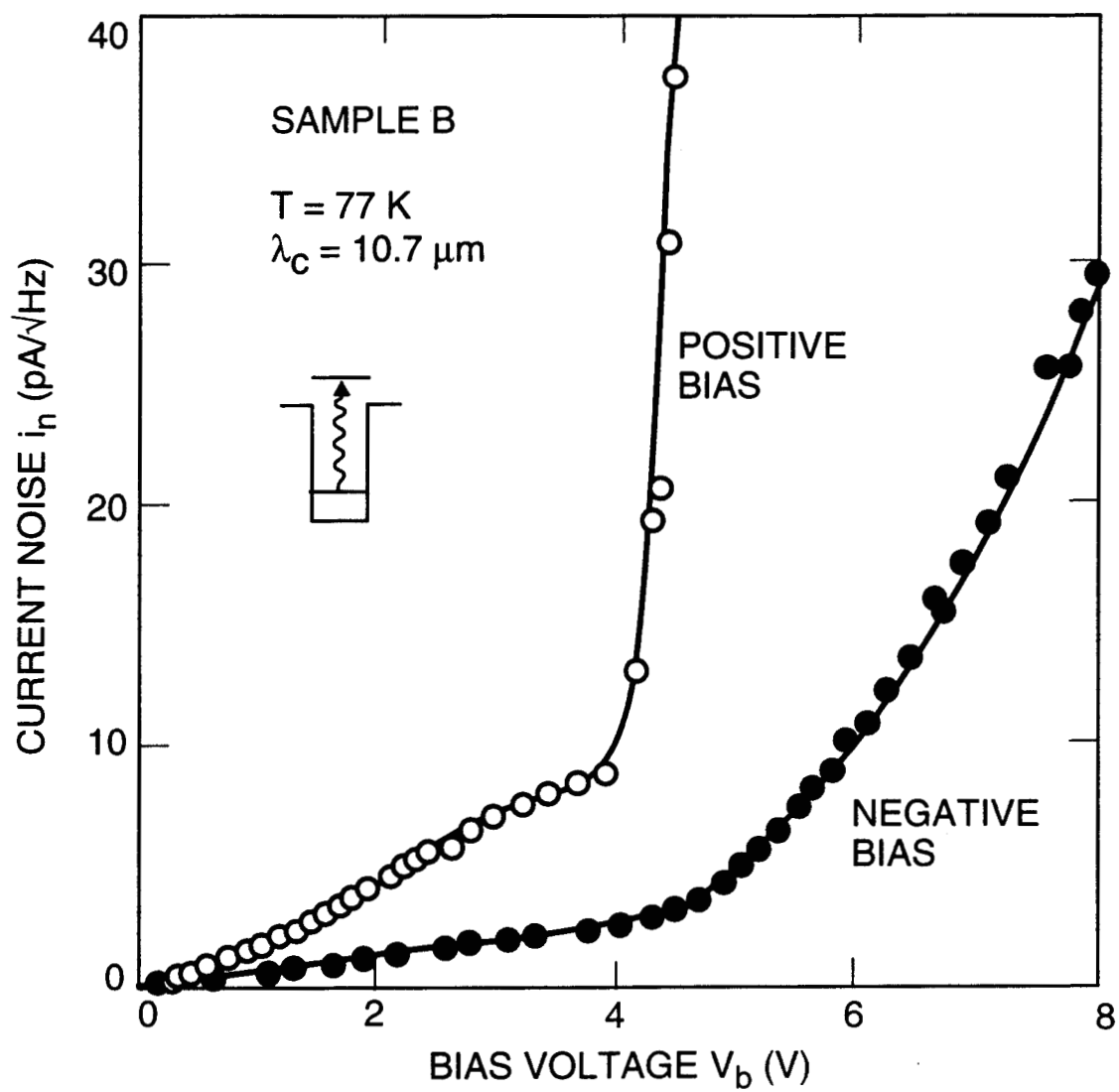












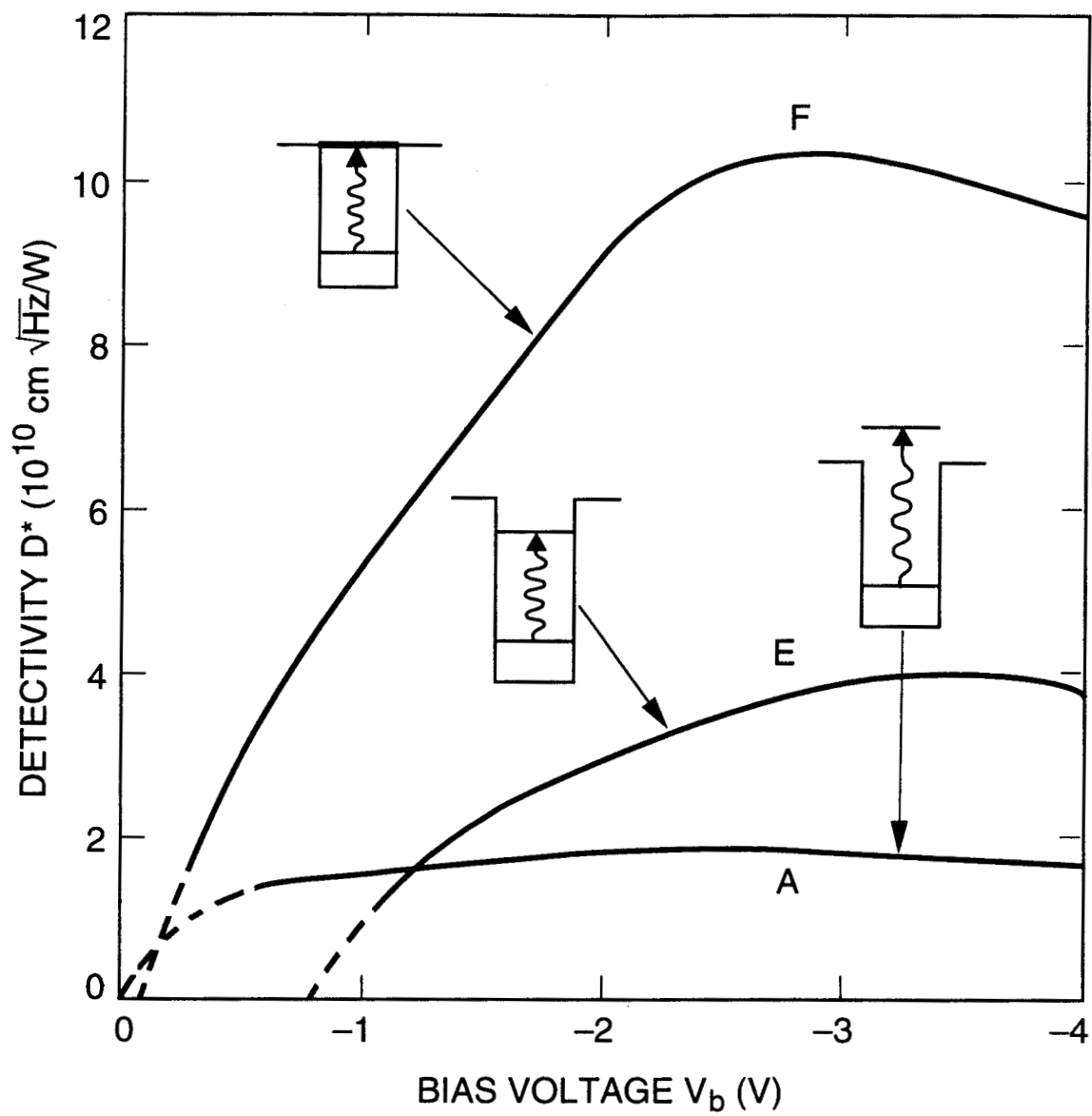


**TABLE I**

Sample	$L_w$ (Å)	$L_b$ (Å)	x	$N_D$ (Å) ( $10^{18}\text{cm}^{-3}$ )	Doping Type	Periods	Intersubband Transition
A	40	500	0.26	1.0	n	50	B-C
B	40	500	0.25	1.6	n	50	B-C
C	60	500	0.15	0.5	n	50	B-C
D	70	500	0.10	0.3	n	50	B-C
E	50	500	0.26	1.4	n	25	B-B
F	45	500	0.30	0.5	n	50	B-QB

**TABLE II**

Sample	$\lambda_p$ ( $\mu\text{m}$ )	$\lambda_c$ ( $\mu\text{m}$ )	$\Delta\lambda$ ( $\mu\text{m}$ )	$\Delta\lambda/\lambda$ (%)	$\alpha_p$ (300 K) ( $\text{cm}^{-1}$ )	$\eta_a$ (300 K) (%)	$\eta_a$ (77 K) (%)	$\eta_{\text{max}}$ (%)
A	9.0	10.3	3.0	33	410	10	13	16
B	9.7	10.9	2.9	30	670	15	19	25
C	13.5	14.5	2.1	16	450	11	14	18
E	8.6	9.0	0.75	9	1490	17	20	23
F	8.9	9.4	1.0	11	451	11	14	20

**TABLE III**

Sample	$\lambda_p$ ( $\mu\text{m}$ )	$\lambda_c$ ( $\mu\text{m}$ )	$\Delta\lambda$ ( $\mu\text{m}$ )	$\Delta\lambda/\lambda$ (%)
A	8.95	9.8	2.25	25
B	9.8	10.7	2.0	20
C	13.2	14.0	2.5	19
D	16.6	19.0	4.6	28
E	8.1	8.5	0.8	10
F	8.4	8.8	1.0	12